



Multi-parameter optimization of gamma emission tomography instruments for irradiated nuclear fuel examination

L. Senis^{*}, V. Rathore, E. Andersson Sundén, Z. Elter, D.M. Trombetta, A. Håkansson, P. Andersson^{**}

Division of Applied Nuclear Physics, Department of Physics and Astronomy, Uppsala University, Uppsala, Sweden

ARTICLE INFO

Keywords:

Gamma emission tomography
Nuclear fuel PIE
Instrumental designing
Pareto optimization

ABSTRACT

Material test reactors have an extended use in irradiation testing of novel nuclear fuel materials and the fuel behavior in off-normal conditions. The performance of the nuclear fuel is examined in in-pile and out-of-pile post-irradiation examinations (PIEs), e.g., using Gamma Emission Tomography (GET). GET is a nondestructive assay that images the internal spatial distribution of gamma-emitting nuclides built up in the fuel due to irradiation. Since GET can be performed close to the reactor and without intrusion in the fuel object, it can potentially speed up the data generation from PIE in irradiation testing.

The performance metrics of GET devices can be identified regarding time requirements, noise in the reconstructed image, signal-to-background ratio, and spatial resolution. However, these are complicated to determine, partly due to inherent trade-offs between the metrics themselves, partly because they depend on the fuel activity and its spectrum (i.e., object dependent), and, finally, on the GET setup and its configuration.

This work proposes a structured methodology for optimizing the collimator design for a new generation of GET tomography setups, intending to improve spatial resolution by one order of magnitude: from the millimeter scale to the hundred-micron scale. The conflicting performance metrics are determined based on the controllable parameters of the GET setup and the uncontrollable parameters of an anticipated fuel object, able to provide a signal-to-background ratio above a customized limit, chosen based on the specific application. The trade-off between the performance remaining metrics is then visualized by a Pareto approach, where dominated solutions are rejected. Finally, constraints on noise level and measurement time are used to find the optimal spatial resolution, without applying noise suppression filters.

Two GET setups are presented using the outlined method. Firstly, to upgrade the tomography test bench BETTAN at Uppsala University, a new segmented HPGe detector is planned to be used with low-activity fuel rod mock-ups. Secondly, a GET system for investigating high-activity nuclear fuel rods of representative burnup. For a nuclear fuel inspection, the results showed that a spatial resolution of about 300 μm is possible with reasonable noise and measurement time constraints.

1. Introduction

Gamma emission tomography (GET) is a passive nondestructive assay technique with application in post-irradiation examination (PIE) of nuclear fuel [1–9]. The method uses the fuel's radiation to acquire information on its state. A setup based on the combination of a collimator and a spectroscopic segmented HPGe detector was chosen for this purpose [10].

In GET, several gamma spectra are acquired in different positions by

scanning the sample laterally and rotationally with a collimated detector [11]. From the spectral analysis, a sinogram [12] can be obtained with the gamma-ray intensity of a particular nuclide of interest in each acquired position. Finally, the sinogram is used to reconstruct images representing the spatial distribution of the gamma-emitting nuclide in the cross-section of the fuel [13].

Past devices, such as the Halden tomograph [2], demonstrated the resolution of features in nuclear fuel rods on the millimeter scale, such as fragments generated as a consequence of Loss-of-Coolant Accident

^{*} Corresponding author.

^{**} Corresponding author.

E-mail addresses: lorenzo.senis@physics.uu.se (L. Senis), peter.andersson@physics.uu.se (P. Andersson).

<https://doi.org/10.1016/j.nima.2023.168698>

Received 20 March 2023; Received in revised form 27 August 2023; Accepted 13 September 2023

Available online 19 September 2023

0168-9002/© 2023 The Authors. Published by Elsevier B.V. This is an open access article under the CC BY license (<http://creativecommons.org/licenses/by/4.0/>).

(LOCA) conditions [14,15]. Effects of interest in such tests include fission-product migration [16], fuel fragmentation, relocation, and dispersal [14], parameters of importance for the safe performance of the fuel in such scenarios.

This work wants to investigate the feasibility of moving the spatial resolution from a millimeter scale to a hundred-micron scale for a new generation of GET devices for PIE. Such development is expected to facilitate small-scale imaging features such as the high burnup rim, highly fragmented transient test fuel, and resolving cladding activation products. It can also be noted that there is currently no other nondestructive PIE technique that can offer insight into, e.g., the radial fission product distribution in used nuclear fuel. Therefore, any progress in this aspect could offer a unique combination of high spatial resolution with low interrogation effort.

The collimator plays a significant role in characterizing the spatial resolution of these devices because it defines the field of view of the setup. In principle, a higher spatial resolution can be achieved by simply reducing the slit size to the desired sub-millimetric scale (as obtained in Refs. [17,18]) and using a smaller step size in the sampling. However, this leads to a decrease in the detector's gamma current, increasing the noise in the reconstruction. In addition, an increased number of samples needs to be acquired, leading to a longer measurement time. A trade-off is present between objectives, such as noise, spatial resolution, and total investigation time. Therefore, multi-parameter optimization is required.

In this work, we propose a structured approach to deal with the optimization task presented, considering trade-offs. As we aim to optimize the spatial resolution, acceptable limits of measurement time and reconstruction noise require simultaneous consideration. Pareto optimization [19] is applied considering those limits and an acceptable signal-to-background ratio using heuristic criteria to choose the sampling frequency. Pareto optimization visualizes the possible compromises between different objectives, which is helpful in the future use of the GET technique, where both the required performance and the pre-conditions of an examination may differ on a case-to-case basis. Further details on the methodology are presented in Section 2.

This work introduces the optimization approach and presents the results of the application on two GET systems. The first application regards the current upgrade of the tomography system BETTAN [20] of Uppsala University, a GET instrument for research and development, using mock-up fuel rods containing Cs-137. Currently, the detector and collimator system is modified to apply multi-channel detection [21,22]. Secondly, we explore the resolution obtainable in the ultimate application of the technique in a realistic scenario with an irradiated nuclear fuel rod inspection.

2. Parameter definition

In this study, we have considered four *performance metrics* of relevance to the purpose of the instrument:

1. Two factors define the spatial resolution: the unsharpness (U), expressed in units of length [mm], and the contrast transfer function (K_{Res}), expressed as resolvable line pairs per millimeter [lp/mm].
2. The total required investigation time (T_{Tot}), expressed in hours [h].
3. The average noise level in the reconstructed images (s) is expressed in the average pixel fluctuations as a percentage of the pixel intensity.
4. The signal-to-background ratio (SBR) is unitless.

Furthermore, we define as *setup parameters*, any parameters of the instrument design or configuration that affect the above performance metrics. Table 1 presents the setup parameters considered relevant for the present study, divided into *controllable* and *uncontrollable* subcategories, indicating which performance metrics they can affect. In Fig. 1, we present a schematic drawing of an experimental setup with an indication of the above parameters for clarification. The importance of

Table 1

The setup and performance parameters are reported, as well as their dependencies. The design parameters represent the characteristics of the setup that can be customized during the instrument's design or selected in the configuration of a tomography scan. Uncontrollable parameters that affect performance are also listed. It can be noted that all the setup parameters influence the performance to some extent due to the conditional dependency introduced by the optimization model. For example, if we change the slit dimensions, it does not change directly the total investigation time. But if we want to maintain certain counting statistics, we need to change the collection time to adjust the count rate variation. In the table, only the direct dependencies are reported.

Controllable parameters	Performance metrics				
	T_{Tot}	U	K_{Res}	s	SBR
Collimator slit dimensions (w_C , h_C and L_C)		X	X	X	X
Collimator materials (μ_C and ρ_C)		X	X	X	X
Lateral step size (l_{Lat})	X		X	X	
Rotational step size (l_{Rot})	X		X	X	
HPGe segment dimensions (w_D , h_D and L_D)				X	X
Center of the object position (d_{CS})		X			X
Collection time (T_{Col})	X			X	
Uncontrollable parameters					
Source dimensions (r_S)	X				X
Source materials				X	
Source activity (A)				X	X
Emission energies (E_γ)				X	X

the detector in defying setup performance was already addressed by previous work [21], and it will be left outside the optimization performed here.

Since some design parameters affect multiple performance metrics, trade-offs between metrics present themselves. In Fig. 2, we illustrated the map of interactions between different setup parameters and performance metrics. We describe the details of each interaction later in Section 3.

3. Method

The performance metrics introduced in Section 2 are now quantified with a dedicated methodology in the current section.

3.1. Total investigation time

The total investigation time represents the time needed to collect data in all the measurement positions. The bigger the object, the more sample steps are needed to complete a full scan. The confining radius determines the number of steps of each linear scan, r_S , of the object, and the lateral step size, l_{Lat} . The choice of step size determines the spatial sampling frequency as, $f_s = 1/l_{Lat}$, which notably is also affecting the resolution, K_{Res} , as will be discussed later in Section 3.2.

The number of steps needed to complete a lateral scan is calculated as

$$N_{Lat} = (2r_S + M_{Lat}) / l_{Lat}, \quad (1)$$

where M_{Lat} is a safety margin to be sure the scan covers the entire object. The number of required rotational steps, N_{Rot} , is determined according to Ref. [23] as $N_{Rot} \approx \frac{\pi}{2} N_{Lat}$ and for each rotational step all lateral steps are taken. The total number of positions acquired, N_{Tot} , is the product of the number of lateral and rotational positions. The time spent per step is the sum of the data collection time per measurement, T_{Col} and the time occupied by the motion of the setup from one position to the next, T_{Mov} . The data collection time regards the real-time data collection. Since the count rate of the system is low, the dead time of the system is deemed negligible, and thus the real-time equals the detector's live time. We made this assumption based on experience from the Halden tomography system, where the count rates in similar usage were about hundreds of counts per second [2]. However, it must be noted that the count rate

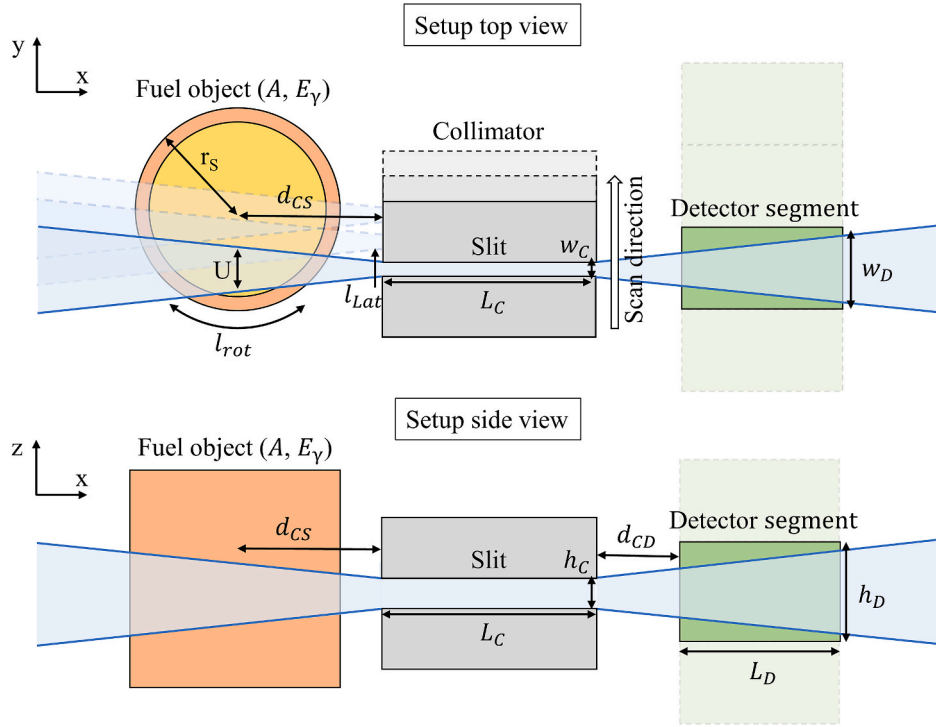


Fig. 1. Schematic representation of the investigation process in GET of a fuel rod. The fuel object is to the left (orange/yellow), the collimator is in the center (grey), and the HPGe segmented detector is to the right (green). The collimator with a rectangular slit is moved in several lateral steps until it scans the entire object. Then the rod is rotated, and the scan is repeated. This process continues until all the rotational steps are performed. In our instrument, multiple detection elements (segments of an HPGe detector) and collimator slits are used to speed up the measurement. The parameters shown in the figure refer to Table 1.

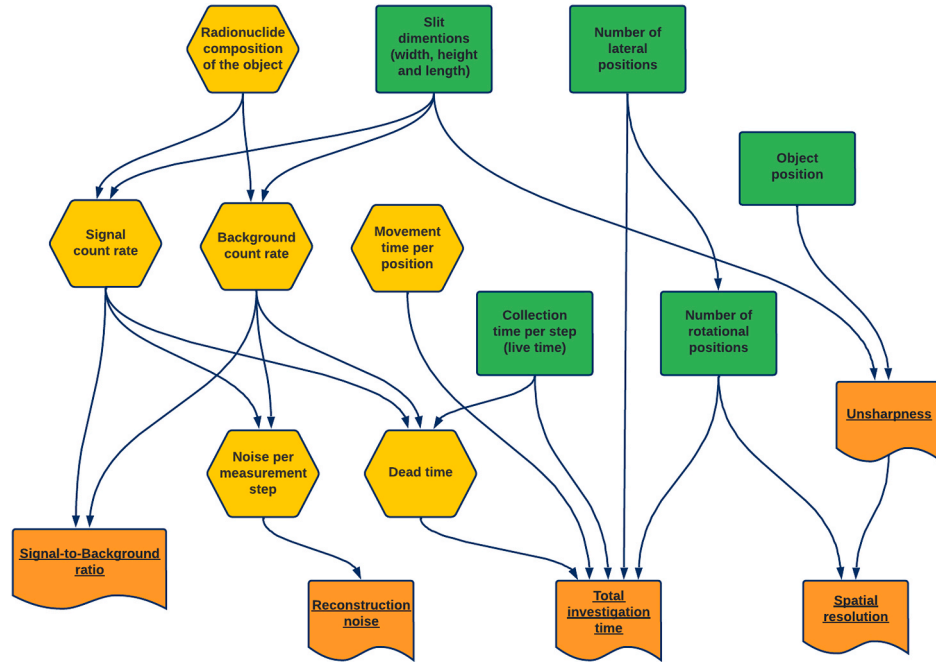


Fig. 2. Identified interactions between controllable parameters (green rectangles), uncontrollable parameters (yellow hexagons), and performance metrics (orange waved rectangles).

may be considerably higher for applications not aimed toward optimized spatial resolution, and larger slits may be used.

The data collection time, T_{Col} , was determined assuming that a certain number of net counts, P , is required in the peak of the nuclide of interest for a measurement position centrally in the sample where the highest intensity is expected to be recorded. The count rate in a central

position viewing a fuel rod is used to correlate the number of counts needed and the data collection time.

$$T_{Col} = \frac{P}{R_{OC}}, \quad (2)$$

The choice of the P also affects the noise level of the reconstructed

image, which is further discussed in Section 3.3 below. We evaluated the count rate in the central position of the fuel sample using the optical contribution proposed in Ref. [24] as

$$R_{OC} = \frac{w_c^2 h_c^2 A_s I_\gamma \epsilon_D}{4\pi L_C^2} \quad (3)$$

and combines the surface source activity concentration, A_s , the relative intensity per decay, I_γ , the detection efficiency, ϵ_D , with the collimator slit dimensions: width, w_c , height, h_c , and length, L_C . The source surface activity has been obtained using the approximation method proposed in Appendix A in Ref. [25] for the center of a fuel rod. In addition, the use of multiple detection elements in our design decreases the T_{Tot} by a factor equal to the number of detection elements, N_{Det} .

The total investigation time, T_{Tot} , is then calculated as:

$$T_{Tot} = \frac{N_{Rot} N_{Lat}^* (T_{Col} + T_{Mov})}{N_{Det}}. \quad (4)$$

It is worth mentioning that R_{OC} as calculated in Eq. (3) would underestimate the count rate, because neglects the penetration component able to cross the collimator through the collimator bulk and, especially, through the slit corners. Nevertheless, this represents a conservative estimation of the total investigation time, with a bias depending on the slit dimensions. As shown in Fig. 6 in Ref. [22], a decrease in the bias can be observed for an increase in the slit length, and tungsten collimators with slits of about 200 μ m, this is expected to be up to 9%.

3.2. Spatial resolution

Two parameters mainly affect the resolution and have been used for its quantification: the unsharpness of the collimator [26], U , and the sampling frequency, f_s .

The unsharpness is the apparent spread [mm] in a scanned projection of a point source. For a collimated device, this depends on the field of view of the collimator slits in the object. If the distance between two features is less than the unsharpness, these will appear smeared in the projection and consequently in a reconstructed image. The unsharpness has been calculated using the primary trigonometrical considerations (Appendix A) to find the spread of the field of view of the rectangular collimator slit (schematically represented in Fig. 1). It depends on the distance between the collimator and the source center, d_{CS} (that needs to be in practice bigger than the object radius) and the collimator slit length, L_C , and width, w_c , as:

$$U = \frac{w_c(2d_{CS} + L_C)}{L_C}. \quad (5)$$

The spatial sampling frequency, f_s , is calculated as the reciprocal of the lateral step, $f_s = 1/l_{Lat}$. According to the Nyquist criterion [27], features with a frequency higher than the Nyquist frequency, $f_{Nyquist} = \frac{f_s}{2}$, will not be possible to be reconstructed. However, the Nyquist criterion represents a theoretical limit that generally is not reached in practical applications due to effects such as unsharpness. Choosing l_{Lat} bigger than U , would lead to an increasing unsampled space between two measurement steps, deteriorating the reconstruction quality. On the other hand, a l_{Lat} smaller than U , may have limited benefit to the spatial resolution, since the smearing effect of the collimator unsharpness will cause neighboring samples to not be independent. Because of this, we have limited our investigation to the step size equal to the unsharpness,

$$l_{Lat} = U. \quad (6)$$

Instead of the Nyquist criterium, a stiffer approach is often used for experimental applications, for example, using the engineering limit $f_{En} = \frac{f_s}{2.5}$, as proposed in Ref. [28]. A series of simulation tests were performed to evaluate the achievable spatial resolution. An object with a concentric spoke pattern, a so-called Siemens star phantom [29], has

been used to test the resolution. The variation of the Michelson contrast (generally used for simple periodic patterns) [30] with the feature frequency in the reconstructions has been used to evaluate the spatial resolution of the setup.

The Siemens star was modeled in dedicated Monte Carlo simulations using the MCNP6 code [31], using a fixed number of spokes. The scanning process using an ideal (absorbing) collimator was simulated in the computational environment, neglecting contributions from outside the slit. The number of lateral and rotational steps used has been calculated as mentioned in Section 3.1, using a step size equal to U (Eq. (6)). The simulated profiles have been organized in a sinogram (Fig. 3a) and used to obtain a filtered back projection reconstruction using the default ‘‘Ram-Lak’’ filter [32,33] (Fig. 3b). From the reconstructed image, a degradation of the Michelson contrast, C , is expected in the center of the object compared to its periphery, because of the increase in the feature frequency. Therefore, the Michelson contrast has been evaluated along the circumference with various radii [34] using the equation:

$$C = \frac{I_{Max} - I_{Min}}{I_{Max} + I_{Min}}, \quad (7)$$

Where, I_{Max} is the average of the highest ten-pixel intensities, and I_{Min} is the average of the lower ten-pixel intensities for each circumference. The frequency of the features has been calculated as the ratio between the number of spokes (fixed at 20) and the circumference [mm]. The frequency increases for circumferences closer to the center, reaching the point where it is impossible to resolve the spokes features anymore. We set the limit to the contrast exploitable at 30% (the upper limit of the contrast interval used in Ref. [29] to estimate the spatial resolution), and we considered features with lower contrast not resolvable.

For every setup simulated, the frequencies corresponding to 30% contrast, f_{30} , were compared to the sampling frequency and used to calculate a correlation factor Q defined as, $Q = \frac{f_s}{f_{30}}$. The results of the resolution test are shown in Section 5.1.

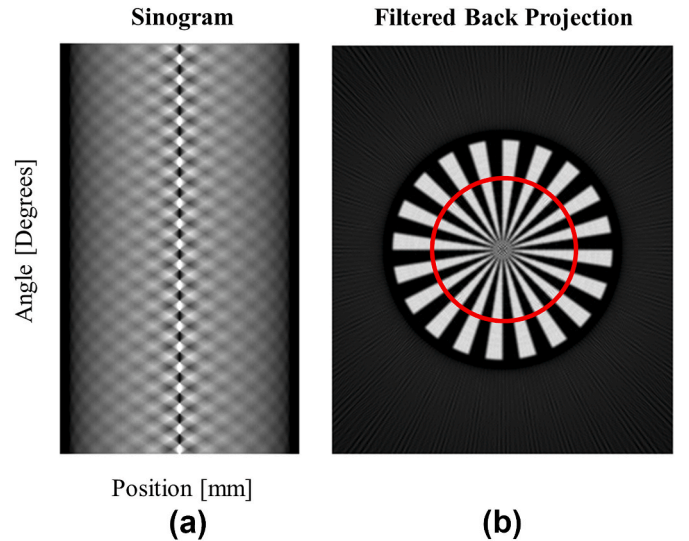


Fig. 3. a) An example of a sinogram obtained from MCNP simulation is shown for illustrative purposes. The simulations have been performed using a perfectly attenuating collimator with a rectangular slit (0.2*5*100 mm), an angular rotation step of 1°, and a statistical cutoff of less than 1% for the positions measured in the central region of the object. b) A reconstructed image of the phantom object obtained with the simulations. In particular, the red circumference represents an example of the circumferences used to calculate the Michelson contrast.

3.3. Reconstruction noise

3.3.1. Noise model generator

The reconstruction noise depends on the counting statistics (defined in the imaging field also as “shot” noise [35]) of the individual radiation measurements [36,37]. Therefore, the number of signal and background counts in the full-energy peak of interest in the spectrum plays a significant role in defining the noise level (s) of the image.

A dedicated cylindrical phantom object was used to predict the noise propagation from measured data to the reconstructed images. This test phantom was modeled assuming, for both the scenarios proposed, a homogeneous activity concentration, assuming that no particular redistribution of the nuclide has occurred (this is especially valid for the mockup rods planned to be used in BETTAN). Having a phantom with a homogeneous initial activity, we could in principle identify any fluctuations of the reconstructed activity as noise. The effect on the image reconstruction noise, caused by a statistical fluctuation expected of the net counts of the peak, P , was then analyzed.

We generated the noisy reconstructions based on the Radon transform method [38] with the following steps:

1. Phantom creation: To meet the requirement of the Radon transform, a rod phantom object with homogeneous activity and an image size $N_{Lat} \times N_{Lat}$ pixels is created, with squared pixels and sides equal to U . The radius of the phantom is equal to the fuel sample radius, r_s .
2. Sinogram creation: The Radon transform is applied using the ASTRA toolbox [32,33] to obtain the phantom sinogram (forward projections).
3. Sinogram normalization: We normalized the sinogram by the number of net peak counts expected in the central position of the fuel sample, P , without considering the self-attenuation effects due to the rod materials. This choice was made to have a rough estimate of s without the impact of inaccuracy caused by self-attenuation.
4. Noise modelling: A Gaussian noise, σ_{Gauss} , was introduced to each data point of the normalized sinogram. The noise fluctuations derive from a combination of the uncertainty of the peak count statistics and the continuum background present underneath. The background has been calculated using the method proposed in Ref. [36] from the predicted measured spectrum (obtained using the method proposed in Ref. [25]). This continuum component could be expected to play a relevant role for short-cooled nuclear fuel samples due to the

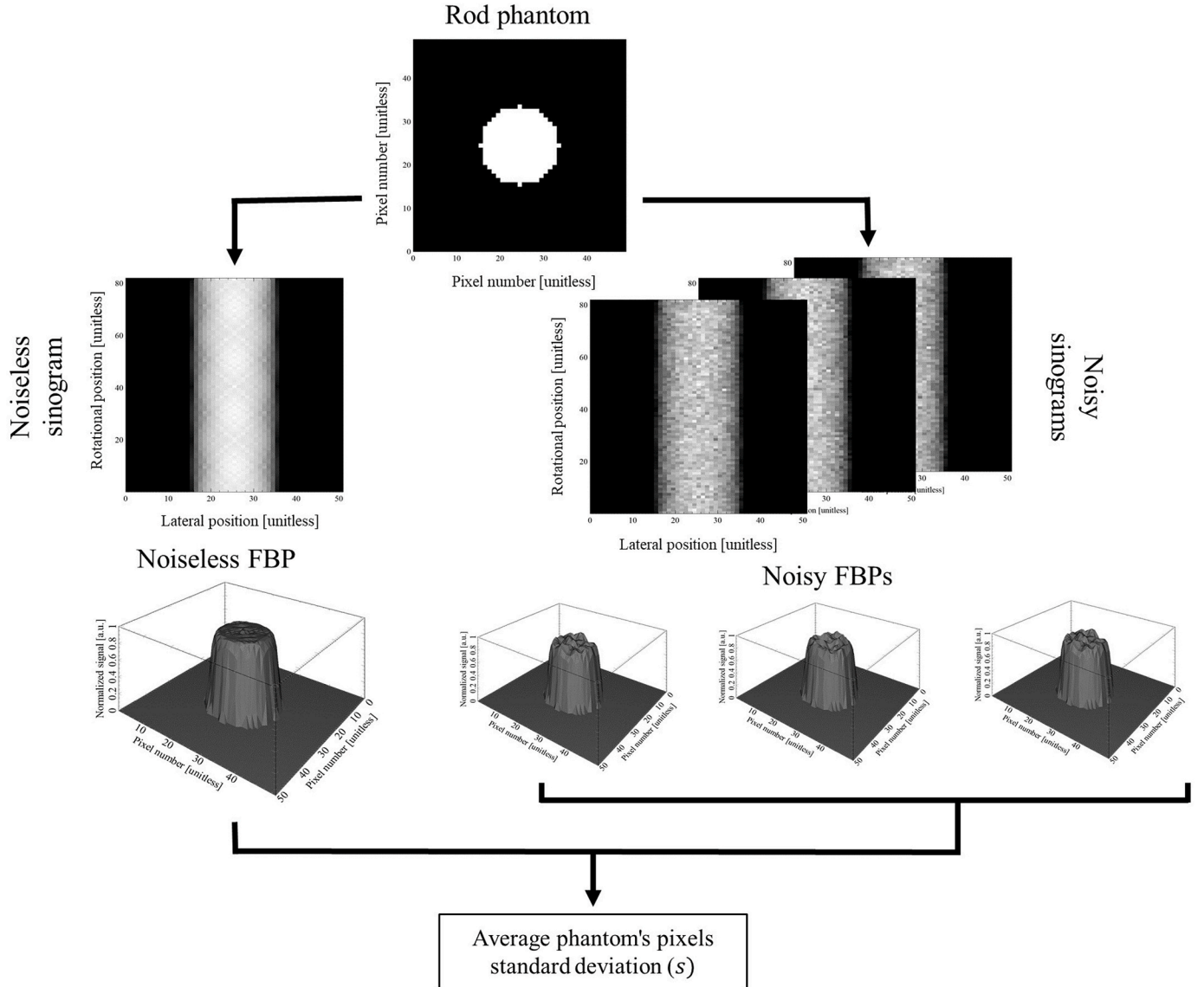


Fig. 4. The flow chart represents the steps used to evaluate the noise level in the reconstructed images. We used the image to generate a reference (noiseless) sinogram and a series of noisy sinograms (obtained to apply Poisson random noise to each pixel). The sinograms were then back-projected, and we evaluated the shot noise as the average of the pixels' deviation between the noiseless and noisy reconstructions. The noisy images used in this figure have s value of about 5%.

interference of high-energy gammas at lower energies. The noise was modeled using the “*normrnd*” function in Matlab: the mean value of the pixel and as standard deviation,

$$\sigma_{\text{Gauss}} = \sqrt{P + 2B}, \quad (8)$$

where B is the number of background counts. We considered the number of counts included in ROI equal to $2 \times \text{FWHM}$ of the peak and an upper and lower background interval, each equal to one FWHM and adjacent to the ROI region.

5. Back-projection: The noisy sinogram is back-projected (also using the ASTRA toolbox) using the default “Ram-Lak” filter [32,33], generating a reconstruction affected by shot noise.

We repeated steps 1-5, producing 20 noisy sinograms for corresponding reconstructed images (the process scheme is shown in Fig. 4). A single image without noise is also generated as a benchmark. The average unbiased standard deviation, s , was calculated between the noiseless reconstruction (used as a reference) and noisy reconstructions. The parameter s was used as a parameter to quantify the average shot noise among all the pixels belonging to the rod phantom.

It can be noted that the method used for the noise quantification does not consider any noise suppression filter to improve the image quality. Any adverse effect derived from the collimator, such as the collimator’s blurring, has also been neglected (the phantom data were procured using a perfect collimation strategy). Regarding noise suppression filters, it can be noted that filters that remove high-frequency noise will also remove high-frequency signals, and thereby inadvertently limit the spatial resolution that we also want to optimize. Therefore, the use of dedicated noise reduction filters should be avoided in this work. This evaluation also neglects the effects derived from the possible nonuniform distribution of the nuclides in the fuel sample, which might locally affect the image noise.

3.3.2. Gaussian process regression model for reconstruction noise generation

A fast noise estimation is required when many iterations are needed, such as during the optimization procedure. A surrogate model based on the Gaussian Process (GP) technique [39] has been proposed with this scope.

The GP model used has been created using the dedicated Matlab function, called “*fitrgp*,” using the “*squaredexponential*” kernel and the training optimized using the “*OptimizeHyperparameters*” function. We trained the GP model using the s distribution generated by the procedure proposed in Section 3.3.1, in a relevant the P and U domain space (the training parameters are shown in Table 5 in Section 5.2). After training, the GP can estimate s and its uncertainty for any given P and U in the range of the training.

Finally, four GP models have been generated: one for the BETTAN application and three for the representative fuel case (one for each nuclide proposed in the study). Section 5.2 below shows the GP model used for Cs-137 as a representative example.

3.4. Signal-to-background ratio evaluation

The background is expected from various sources, including natural background, continuum background from higher energy gamma rays (in the case of realistic fuel objects), and gamma rays from the object that penetrate the collimator bulk material. The continuum background mainly affects the low-energy region of the spectrum, possibly affecting the peaks’ detectability. It also generates additional uncertainty in the peak counts’ evaluation (which is propagated as noise in the reconstructed image).

Of particular concern for the design is the background from the fuel that may penetrate the shielding of the collimator since fuel objects are strong gamma-ray sources. Since the damping of gamma rays in the

collimator bulk can be controlled by appropriate design, this background component has been evaluated.

Two cases can be considered. The scattered build-up, which causes a lower energy component, can largely be discriminated from the signal energy due to the excellent energy resolution of HPGe. Secondly, due to the penetrating nature of gamma radiation, the full-energy background may pass through the collimator bulk without interaction. The latter is of particular concern since it is indistinguishable from signal energy. Providing a metric to quantify the penetration component is necessary for two main reasons:

1. Help in establishing criteria to limit the length of the collimator (otherwise it could be made arbitrarily short).
2. Keep the penetration component at a low intensity, or it may degrade the reconstruction (as it would provide an unwanted signal even in measurement steps where no fuel is in sight of the detector).

We estimated the extent of this leakage component using the Beer-Lambert law [40]. The fuel sample was considered a point-like object with all its activity, A , and the collimator as a solid block with no slit. Depending on the collimator material, the corresponding mass attenuation coefficient (excluding coherent scattering), $\mu_C(E_\gamma)$, and density, ρ_C . Both the detector and the source were, for simplicity, considered adjacent to the collimator, and the solid angle of the detector, Ω_D , is,

$$\Omega_D = 4 \arcsin \left(\frac{w_D h_D}{\sqrt{(4L_C + w_D)^2 + (4L_C + h_D)^2}} \right), \quad (9)$$

calculated using the formula proposed in Ref. [41]. The count rate of the leakage component, R_{LC} , was evaluated as:

$$R_{LC} = A \varepsilon_D \frac{\Omega_D}{4\pi} \exp(-\mu_C(E_\gamma) \rho_C L_C), \quad (10)$$

assuming that the solid angle is small enough, the length of the gammas’ path in the collimator can be considered constant, equal to the length of the collimator, L_C . The ratio between signal and leak-through background, $SBR : \frac{R_{oc}}{R_{LC}}$, was used to set a constraint on the solutions considered acceptable.

4. Design of a tomography test-bench

4.1. BETTAN setup

GET test benches such as BETTAN and others [42] help investigate new tomographic techniques and detector equipment and provide test data for reconstruction algorithms without requiring irradiated nuclear fuel [20,43]. Mock-up fuel rods are used instead to obtain radioactive test objects since such are easier to access and handle in most labs.

BETTAN, shown in a schematic drawing in Fig. 5, is currently planned for a test with a novel segmented High Purity Germanium (HPGe) detector concept [21,22] combined with a multi-slit collimator. The mock-up rods of BETTAN have titanium cladding filled with granulated copper activated with Cs-137 [43]. We listed the detector parameters and the mock-up rods in Table 2.

As shown in Table 1, all the setup parameters in the model contribute to some extent to the setup performance. However, among these, a particular distinction needs to be made for the collimator. The collimator design plays a significant role in all the performance metrics discussed in Section 3, and the method proposed in this work focuses on its optimization.

4.2. Design constraints for BETTAN optimization

For the BETTAN application, the constraints that play a role in the collimator are listed below:

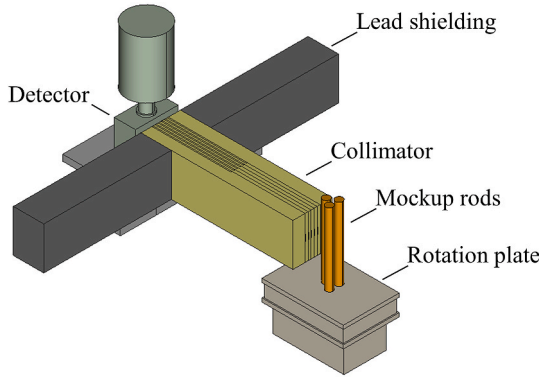


Fig. 5. CAD representation of the BETTAN setup. A mock-up fuel rod is positioned on a rotating magnetic plate and rotated at the desired angle. A multi-slit collimator is positioned on a bench that can be translated laterally. On either side of the collimator, two lead blocks are added to provide additional shielding from the sources. A segmented HPGe detector is positioned behind the collimator, and its segments are aligned with the collimator slits.

Table 2

The table summarized the measurement parameter of BETTAN, in particular, the dimension of the detector and its segments [22] and the mock-up rods used as samples.

BETTAN parameters	
Source active height	102 mm
Source active radius	5.25 mm
Cladding thickness	0.75 mm
Average source activity per rod	313 MBq
Collimator center source distance	35.25 mm
Collimator detector distance	20 mm
Detector segment height	10 mm
Detector segment width	5 mm
Detector segment depth	30 mm
Detector efficiency at 661.7 keV	~14% [22]
Number of segments	6
Motion time per step	5 s

1. Measurement time: The total measurement time must be practical regarding the use of the workforce and occupancy of the instrument. In the following analysis, we considered a time constraint of 24 h, representing a conservative constraint (the maximum refilling interval for the liquid nitrogen-cooled detector is 48 h).
2. Detector dimensions: The collimated beams must hit within the respective detector segments, implying restrictions for the collimator slit width and divergence. The vertical divergence is, in particular, affecting the height dimension of the collimator slit since the width of the slit is, in practice, limited by the desire for high spatial resolution. Using trigonometrical relations (Appendix A), the slit height, h_c , can be calculated using the following expressions:

$$h_c = \frac{(h_D - 2M_h) L_C}{L_C + 2(d_{CD} + L_D)}, \quad (11)$$

where $2M_h$ is the total margin considered (10% of the total detector segment height) between the segment boundary and the beam spot (to account for possible misalignments), and d_{CD} is the collimator-detector distance.

3. Source dimensions: The distance from the collimator face to the fuel center, d_{CS} , needs to be bigger or equal to the fuel radius, r_s .
4. Lateral step: The fixed segmentation of the detector allows the investigation of 6 steps simultaneously. When performing a lateral scan, the system moves the detector progressively till it reaches the position covered by the first step of the neighbor segment. When this happens, the setup has already scanned a length of 3 cm. The

limitation mentioned above in the lateral step affects the scanning investigation time for more extended objects.

5. Rotational step: The number of rotational steps in BETTAN is currently limited to only integer values of the rotation angle (in degrees).
6. Source activity: We considered the source activity of a single mock-up rod to evaluate the detector signal, which is relatively low compared to a representative irradiated fuel case used for the previous GET use on LOCA test rods in the Halden reactor.
7. Signal-to-Background ratio (SBR): The method provided in Section 3.4 allows the calculation of the SBR for different combinations of collimator lengths and materials. This parameter has not been included in the optimization methodology and has been treated instead as a constraint. For BETTAN, an $SBR \geq 100$ has been deemed sufficient. The results (presented in Section 5) show that a few percent of noise in the reconstruction is expected for a net peak of a few hundred counts. With an SBR of 100, this would keep the predicted penetration component in the order of a few counts unit and has been considered acceptable for this application. For the PIE case, one order of magnitude as an additional margin has been considered because of the higher fuel activity and energy of the gamma lines involved. Nevertheless, this parameter will be further integrated into a future version of the optimization methodology, also according to the specific requirements of the investigation.

4.3. PIE fuel scenario

The spatial resolution obtainable in test benches, such as BETTAN, may not present substantial progress toward resolution in the 100 μ m range. It should be noted that this is mainly a consequence of the limited activity of the rod mock-up source term. In the case of irradiated fuel, depending on burnup history and cooling time, the higher source term compensates for such an effect. Therefore, an estimate of the optimal spatial resolution achievable using the GET technique for PIE on actual nuclear fuel is proposed.

In such a scenario, to obtain a relevant example source term, a gamma fuel spectrum was calculated for a typical Swedish PWR fuel irradiation history [44]. Using the methodology proposed by Ref. [25], an infinite pin-cell reactor was modeled in SERPENT2 [45] using a rod of UO_2 fuel of 4.1 mm radius with a Zirc-4 [46] cladding of 0.6 mm of thickness. The depletion calculation was performed for four reactor cycles of 340 days (cycle downtimes of 24 days/cycle) for a cumulative burnup of 46 GWd/tU at the end of the operation. We assumed the fuel would be subjected to a tomographic investigation after 14 days at the end of the fourth cycle. It should be mentioned that the anticipated use of the proposed high-resolution GET is at research reactors. However, we choose the burnup scenario to obtain a typical source activity.

Considering the high activity of a realistic irradiated fuel, we considered a high attenuating material such as Densimet® 180. The leakage component, R_{LC} , has been calculated using Eq. (10) and considering the emission of 1000 gamma lines with the highest activity emitted by the rod. We used the activity within 1 m of the rod closest to the collimator for the SBR calculation. The segmented detector response has been included using dedicated MCNP6 simulations with a mono-directional point source to mimic the collimated beam hitting the detector, as described in more detail in Section II-D in Ref. [25].

The study was focused on the reconstruction of three nuclides, listed in Table 3, that demonstrated their utility in previous investigations as indicators of specific fuel parameters, such as the burnup (Cs-137) [47] and the power distribution (La-140) [48]. We also included Nb-95, representing the highest gamma emitter observed in the fuel spectrum in the proposed scenario, offering the best spatial resolution.

4.4. Optimization

The dimensional parameters shown in Fig. 1 are subject to

Table 3

The table compares the activity of Cs-137 per unit length of the BETTAN's mock-up rods and the activity of Cs-137, La-140, and Nb-95 expected for a freshly irradiated fuel rod obtained from SERPENT2 depletion calculations. It can be noted that for Cs-137 (which is present in both objects), the activity in the fuel is three orders of magnitude higher.

	Mock-up rod BETTAN	Irradiated fuel case from SERPENT2 simulations [45]		
Nuclide	Cs-137	Cs-137	La-140	Nb-95
Gamma-line [keV]	661.7	661.7	1596.2	765.8
Activity per unit length [Bq/cm]	3.04E+07	2.29E+10	8.46E+10	1.55E+11
Photon intensity [ph/ cm/s]	2.74E+07	2.07E+10	8.07E+10	1.54E+11

optimization. These are L_C , w_C , h_C , d_{CS} , L_D , w_D , h_D , and d_{CD} . However, the three spatial dimensions of detector segments (L_D , w_D , h_D) are already fixed using a predesigned detector and are excluded from this optimization.

Since the vertical resolution is not prioritized (exploiting the symmetry of rod objects), it is rational to maximize the count rate, maximizing the slit height, h_C . However, it is clear from constraint n° 2 in Section 4.2 that it needs to be limited to irradiate only the target segment of the slit. From Eq. (11), it is clear that the maximum h_C is found by minimizing the distance from the detector to the collimator, d_{CD} . Due to the space required for detector casing, the minimum distance d_{CD} between the active volume of the segment and the collimator is 20 mm. With d_{CD} fixed, h_C is determined by L_C according to Eq. (11).

Similarly, d_{CS} is minimized, due to its reciprocal relation to the unsharpness, U , as seen in Eq. (5). Since no other performance metric is affected by d_{CS} , it is plain to see that it should be minimized. However, it is limited by constraint n° 3 (Section 4.2), by the size of the object under consideration, with a certain margin. In the calculations, d_{CS} has been considered equal to 30 mm plus the active radius of the sample object (5.25 mm for BETTAN and 4.1 mm for the fuel scenario).

Having optimized setup parameters that do not present a trade-off between different performance metrics. We remain with two free-dimensional parameters, L_C and w_C to optimize. Here, we generated many possible combinations and ranked them according to their performance metrics. For the optimization proposed in Section 5.2, 6.9E+05 possible setups were generated.

For practical reasons, in the generation of setups, the parameters varied are the unsharpness and the collimator length (U and L_C). Having already minimized d_{CS} , the unsharpness, U , is uniquely determined by L_C , and w_C , and therefore a coordinate transform between the w_C and L_C to U is possible as,

$$w_C = \frac{UL_C}{(2d_{CS} + L_C)}. \quad (12)$$

The motivation for using the U - L_C coordinates for the setup optimization is that U is possible to map to the spatial resolution, as described in Section 3.2, while L_C is an essential input in the Signal-to-Background evaluation according to Section 3.4.

In addition to the dimensional parameters, a free parameter related to the time of data collection needs to be varied. For this purpose, we vary the parameter P , the number of net counts collected in a central position of the rod object.

The optimization procedure was applied as the following:

1. Design generation: We generated the collimator designs with a specific range of unsharpness values ($0.2 \text{ mm} < U < 1.5 \text{ mm}$) and collimator lengths ($50 \text{ mm} < L_C < 300 \text{ mm}$) and the correspondent, h_C and w_C have been obtained using Eqs. (11) and (12).
2. Count rate estimation: We used the collimator designs generated from step 1 to calculate the expected central position count rate,

using the detector efficiency and the collimator response described in Eq. (3).

3. Central position counts variation: The P parameter has been varied between an upper to a lower limit by a fixed step. The upper limit is set and deemed sufficient for a good reconstruction precision (e.g., 400 counts for BETTAN application). In contrast, we set the lower limit to the value of P to get an s equal to 10%, according to the GP estimation described in Section 3.3.

For each value of P , the steps a, b, and c below are performed:

- a) Total time constraint application: The collection time, T_{Col} , has been calculated using Eq. (2) considering the count rate expected and the number of counts needed, P . The T_{Col} combined with the number of lateral steps (Eq. (1)) and rotations and the number of detector segments was used to calculate the total investigation time, T_{Tot} , using Eq. (4), and values obtained selected according to the time requirements of the investigation (e.g., 24 h).
 - b) SBR constraint application: We evaluated the signal-to-background ratio SBR for each collimator design. The solutions with a value above the limit were considered acceptable (100 for BETTAN and 1000 for the fuel scenario).
 - c) Reconstruction noise estimate: For the subset of the acceptable solutions (fulfilling both T_{Tot} and SBR constraints), the reconstruction noise, s , has been calculated using the GP model trained (as described in Section 3.3.2) in the domain of interest of the application.
- 4 Pareto front generation and design choice: Once calculated s for the pool of the solutions fulfilling the constraints, a sorting routine was applied to select, for different noise levels, the design solutions that provided the smallest unsharpness. From the sorting procedure, a curve of non-dominated solutions called "Pareto front" was obtained, showing the best unsharpness achievable as a function of the noise level. Finally, depending on the application, a specific design can be chosen according to the acceptable noise level.

Note on the noise limits: the value of s should be chosen considering the specific application aimed for. For example, we can expect that for localization of fragmented fuel in transient tests, higher noise can be tolerated than, e.g., determining the fuel's radial burnup profile. So, the noise limitations should be chosen accordingly.

5. Results

The section presents the results obtained in this work regarding the spatial resolution response and the collimator optimization for the experimental cases proposed in Sections 4.2 and 4.3. A summary of the parameters and how they have been treated in the model is reported in Appendix B.

5.1. Siemens star resolution tests

In this section, we present the results of the method discussed in Section 3.2 to evaluate the contrast variation for the simulated Siemens star phantom (Fig. 3). The contrast evolution is shown in Fig. 6a as a function of the frequency of the features. We can notice that the unsharpness (here set equal to the lateral step length) is closely correlated with the achievable spatial resolution.

The contrast is stable around 1 for feature frequency lower than 0.2 lp/mm, meaning the setup can resolve them with 100% contrast. Nevertheless, with the increase of the features' frequency, the contrast decreases, at first monotonically, and later it shows a slight increase, which is a sign of spurious resolution. As mentioned in Section 3.2, we considered features presenting a contrast of 30% to be resolvable by the system and the respective line pair frequency to quantify the resolution of the setup. The feature frequency at 30% contrast, f_{30} , was obtained by the cubic spline interpolation function provided in MATLAB [49]. The ratio, Q , between f_S and f_{30} are reported in Fig. 6b. To establish a

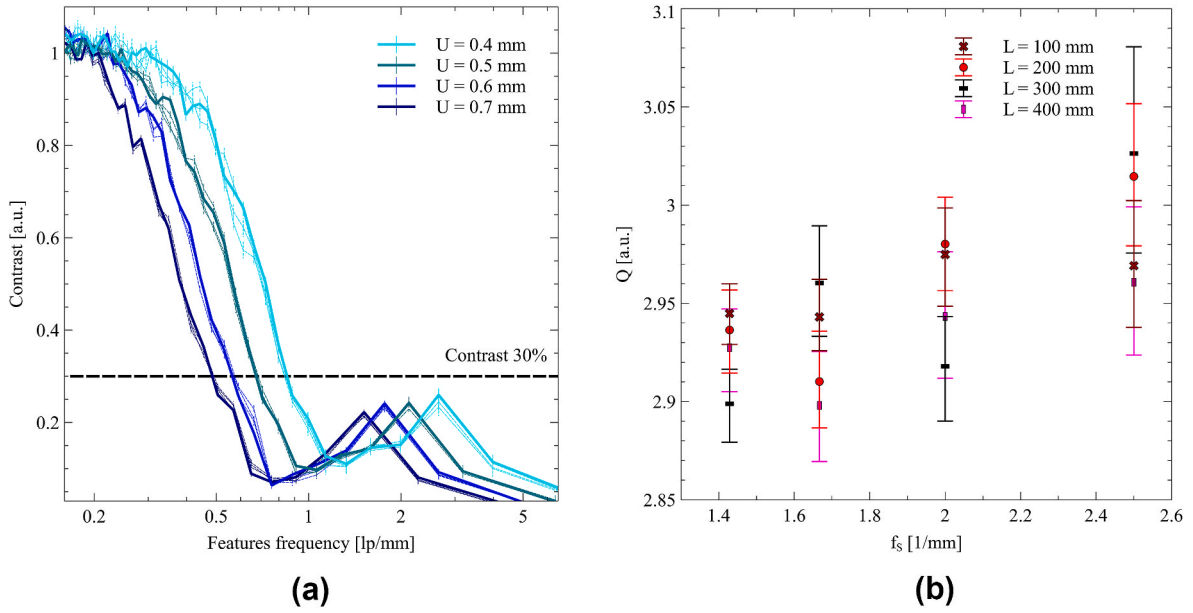


Fig. 6. a) The contrast transfer functions obtained from the simulations for the different U and L_c . In solid shades, we reported the results for setups with U of 0.4, 0.5, 0.6, and 0.7 mm with a $L_c = 100$ mm. Other L_c (200, 300, and 400 mm) are reported in the same color but with dashed lines, showing the same trend as the correspondent curves. The slit dimensions used for the simulations are reported in Table 4 b) The plot shows the Q factors calculated using the definition provided in Section 3.2, using the f_{30} value extrapolated from each curve in a) and the sampling frequency, f_s , calculated from the U values. The uncertainty of MCNP is reported with 1σ .

correlation between f_{30} and f_s , the average was calculated among all the simulations, $\bar{Q} = 2.95$ with a relative error of 1%, which was henceforth used to predict the resolution of the spatial frequency resolvable at 30% contrast for each evaluated design. The uncertainty on Q is therefore affecting the spatial resolution estimate for the same relative error.

It can be noted that compared to the Nyquist frequency, we get a Q value that differs slightly by a small factor (about 1.5), possibly due to the unsharpness.

5.2. Gaussian regression process model

As described in Section 3.3.2, four Gaussian Process (GP) models have been used for the fast calculation of the reconstruction noise expected, s . The training has been performed using different 2D input data sets (based on a combination of U and P values). In Table 5, we reported the value ranges used for the training and their step interval for each application case.

An example of the GP fit model used to calculate s for Cs-137 (for the fuel PIE scenario proposed in Section 5.4) is shown in Fig. 7a, as well as the training data points used. To better show the model accuracy, in Fig. 7b, a set of s random test values (not included in the training) has been plotted in comparison with the s values predicted for the same input values of U and P . The number of events used for the test is about 60% of those used for the GP training (1029). The magnitude of the discrepancies observed is between $\pm 10\%$ of the s of reference, and this discrepancy has been considered acceptable for this application. The

Table 4
summary of the slit dimensions used for the simulations presented in Fig. 6.

L_C [mm]	100	200	300	400	
h_C [mm]	4.50	6.00	6.75	7.20	
w_C					
U [mm]	0.4	0.23	0.29	0.32	0.34
	0.5	0.28	0.36	0.40	0.42
	0.6	0.34	0.43	0.48	0.50
	0.7	0.40	0.50	0.56	0.59

Table 5

Summary of the input parameters used to train the GP model for the four cases proposed.

GP model	U interval [mm]	U step [mm]	P interval [counts]	P step [counts]
BETTAN application	0.2 - 1.5	0.025	34 - 400	3
Fuel case - Cs-137	0.2 - 0.7	0.025	60 - 1500	30
Fuel case - La-140	0.2 - 0.8	0.05	40 - 2000	20
Fuel case - Nb-95	0.2 - 0.8	0.05	40 - 3000	20

uncertainty provided as output from the GP has also been used to estimate the uncertainty of s in the optimization.

5.3. Pareto solutions and BETTAN design selection

The procedure proposed in Section 4.2 is applied to identify the Paretian optimal setups for specific T_{Tot} and SBR constraints. A set of hypothetical setups has been generated by sampling the unsharpness and the collimator length among a certain interval (reported in Table 6). For each combination of U and L_c a corresponding value of the slit height, h_c , and slit width, w_c were calculated using Eqs. (11) and (12) (see Fig. 8a and b).

The dimensions of the collimator (w_c , h_c and L_c) in combination with the source activity, the detector efficiency (provided in Table 2) and the P -value, were used to calculate the total investigation time (using Eqs. (1)–(4)) for each combination of setup and P -value generated (P -step equal of 3 counts). The Paretian optimal solutions were obtained by sorting the setups, selecting the ones that provided a full investigation within selectable time constraints, an SBR above the constraint ($SBR \geq 100$, correspondent to a leakage contribution below 1%), and the best spatial resolution for the same noise level. The collection of these Paretian optima can be visualized as a Pareto surface, as shown in Fig. 9a, by plotting in a 3D space the performance parameters (T_{Tot} , K_{Res}

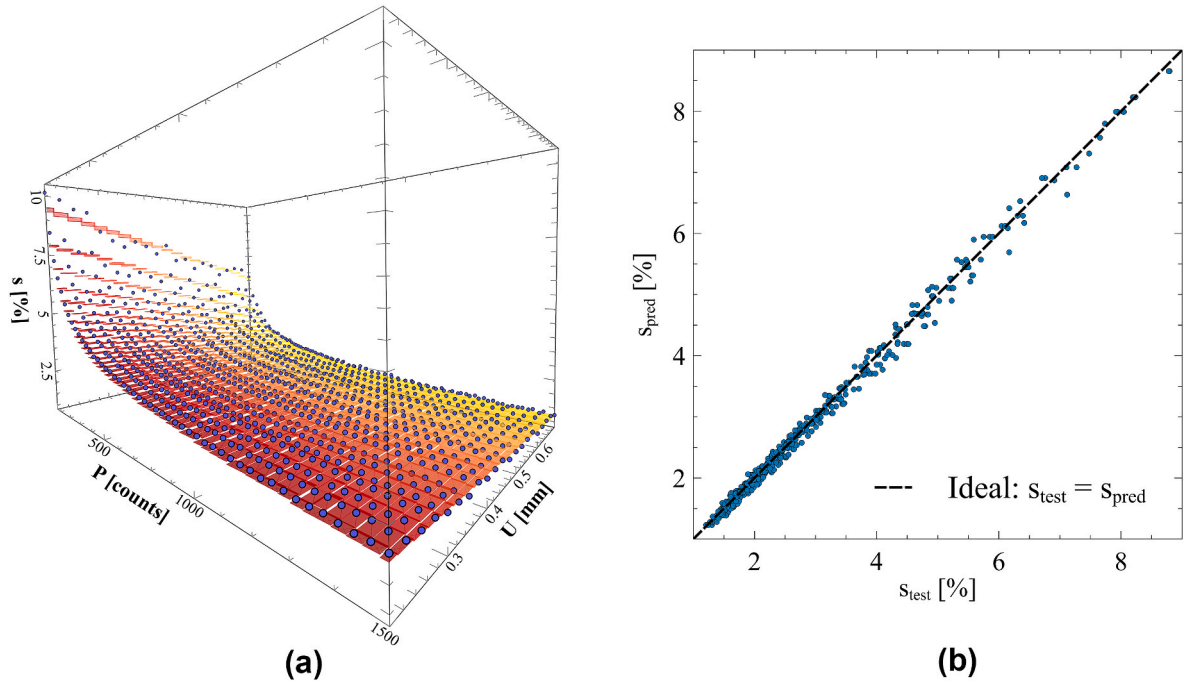


Fig. 7. a) As a representative example, the GP model used for Cs-137 optimization is reported. In purple, dots represent the point generated to train the GP, while the red-shaded surface represents the GP prediction fit. b) The plot shows the agreement between the s test values and the s values predicted by the GP model.

Table 6

Summary of the performance parameter of the selected solution for BETTAN collimator.

Parameter	Optimized solutions	
Collimator material	Structural steel – S355	
Unsharpness - U	0.2-1.5 mm	
Collimator length - L_C	50-300 mm	
Central counts - P	50-400	
Time constraint - T_{Tot}	24 h	48 h
SBR constraint	>100	
Noise level - s	3%	
Number of segments - N_{Det}	6	
Total measurement steps - N_{Tot}	1716	2280
Data collection time - T_{Col}	~297 s	~450 s
Spatial resolution - K_{Res}	0.37 lp/mm	0.43 lp/mm
Slit design selected - $w_C \times h_C \times L_C$	$0.7 \times 6.2 \times 222$ mm	$0.6 \times 6.3 \times 228$ mm

and s) of each optimal design. We reported the spatial resolution in the plot in line pairs per mm [lp/mm], calculated using the conversion factor Q obtained from the simulations (Section 5.1).

In the study, we considered two candidate materials to calculate the SBR: structural steel 355 (S355) and Densimet® 180 (D180) [50]. The material plays a relevant role in the choice of the setup design. Due to its high attenuation properties, Densimet® provides a significant advantage, having for less than half of the length the same attenuation properties of a collimator made of S355. However, for BETTAN, steel still represents a good choice. A collimator of about 200 mm in length can easily fit into the test bench, and it is easier and cheaper to purchase and machine in a multi-slit collimator. These factors make S355 the choice, despite the somewhat better performance of Densimet®. However, it should be noted that depending on the application, higher or lower noise levels may be acceptable, influencing the design of the setup.

From the Pareto surface plot, 2D Pareto fronts can be isolated with solutions that fulfill specific performance conditions. In Fig. 9b and c, we showed two examples of Pareto fronts correspondent to the setups with T_{Tot} of 24 h (red curves) and for the setups that provided a noise level, $s = 3\%$ (green scatter plot). The slit designs corresponding to 2D Pareto fronts are plotted in Fig. 9d and e, using the same reference colors.

The plots of Fig. 9a, b, and 9c show the inherent trade-offs between measurement time, spatial resolution, and noise in the design of a GET system. In principle, many hypothetical designs are optimal, depending on the prioritization between the different objectives; time, resolution, and reconstruction noise. For the BETTAN design, we selected a steel collimator (S355) with a slit cross-section of 0.7×6.2 mm and a length of 222 mm. This setup offers the optimal unsharpness (about 0.9 mm) for a time constraint of 24 h and a noise level of about 3% (P about 300). The spatial resolution of this design is estimated to be 0.37 lp/mm, which will allow for resolution features of the activity distribution of about 1.4 mm. The solution suggested is represented as an orange star-shaped pointer in Fig. 9 and can be tracked through the different parameter domains. In case one of the metrics is insufficient for the desired application, the method gives further indications to the designers on how to improve the performance by acting on the setup design. An example in this application would be to improve the spatial resolution to 0.43 lp/mm (1.2 mm feature resolution) by reducing the slit width to 0.6 mm for an equal reconstruction noise level and 48 h for the investigation. The results are summarized in Table 6.

5.4. Spatial resolution prediction in irradiated fuel scenario

The optimization methodology is now applied to a realistic PIE scenario, proposed in Section 4.3. The optimized solutions were limited to a T_{Tot} of 24 h, starting one examination daily and leaving it running autonomously overnight is considered practical. We reported the noise level expected for the different nuclides in Fig. 10 as a function of predicted K_{Res} . As expected, we obtained a higher resolution for the higher-intensity nuclides. Features with a frequency of about 1.6 lp/mm can be resolved (with about 30% of contrast) for Cs-137 with $s < 5\%$, expected to resolve variations in local activity with the size of about 310 μm . For La-140 and Nb-95, such resolution is higher and is about 2.0 and 2.4 lp/mm, respectively, with the corresponding resolution of local variation of 250 μm and 210 μm . The results are summarized in Table 7.

It can be noted here that La-140 and Nb-95 have relatively short half-lives (respectively, 1.7 d and 35 d) and thus will mostly be present in fuel during their in-reactor life at equilibrium concentration. Note, however,

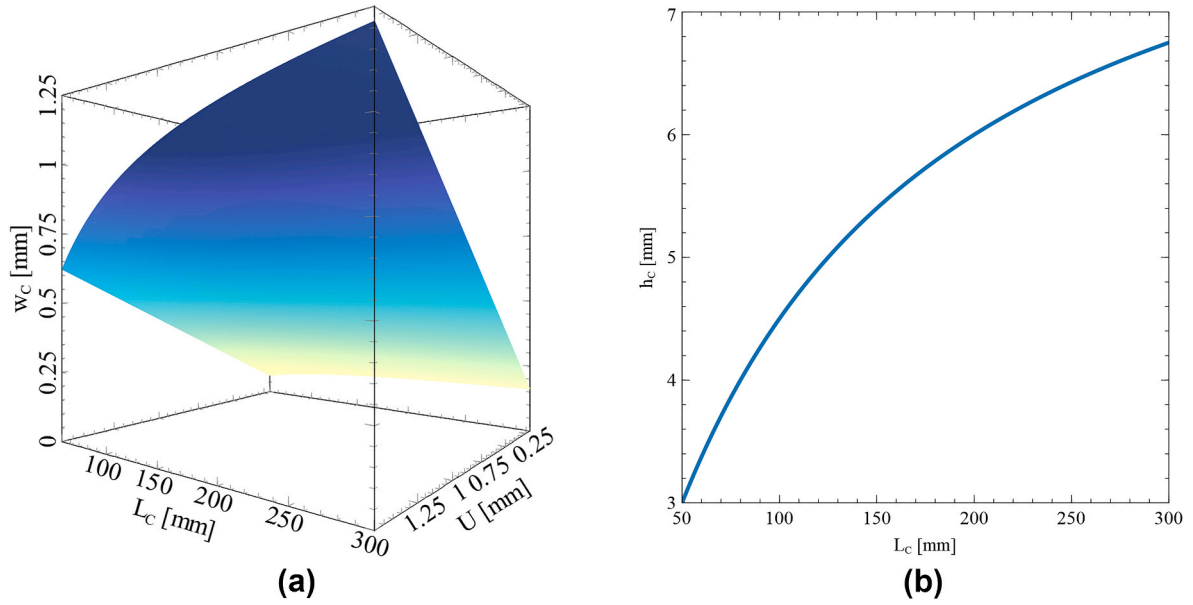


Fig. 8. The slit dimensions generated by all the possible combinations of U and L_C given as input. a) The collimator slit widths (w_C) are reported as a surface plot as a function of unsharpness (U) and collimator length (L_C). b) The collimator slit height generated as a function of L_C .

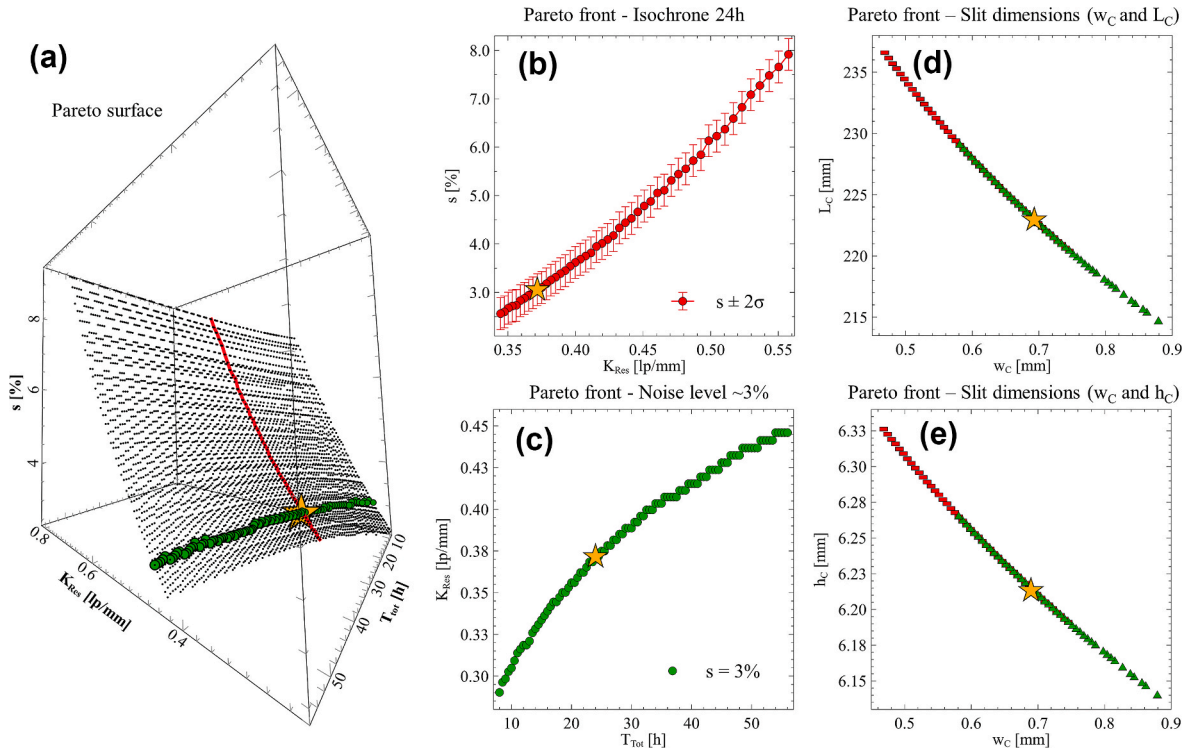


Fig. 9. a) The 3D plot represents the Pareto surface generated by plotting the performance parameters of T_{Tot} , K_{Res} and s for the optimal solution investigated considering the BETTAN parameters shown in Table 2 and a collimator made of S355. b) The Pareto solutions correspondent to a $T_{Tot} = 24$ h have been isolated and plotted as a function of the K_{Res} . c) The K_{Res} is plotted as a function T_{Tot} for the solution with $s = 3.0 \pm 0.2\%$. d) The slit designs correspondent to the Pareto fronts reported in b) and c) are plotted in two 2D graphs using the slit dimensions, respectively (w_C and L_C) in d) and (w_C and h_C) in e) as coordinates for each point. A star-shaped orange pointer has been used to track the solution suggested for BETTAN among the different Pareto fronts in the metric and slit dimension domains.

that their concentrations are also governed by their mother nuclides Ba-140 (12.75 d) and Zr-95 (65 d), respectively. Therefore, these should be available in low and medium burnup fuel, as long as interrogated after a short cooling time. On the contrary, long-lived Cs-137 (30 y) accumulates nearly linearly with the burnup but remains after a long cooling time. Possible corrections can be included to account for the extension of

the collection time in cases where more protracted investigations are feasible. Such corrections would compensate for the signal reduction due to the nuclide decay during the interrogation and keep the contribution to s constant with the progress of the investigation.

It can be noticed that the optimal resolution estimated in the study does not represent the ultimate resolution achievable for GET devices.

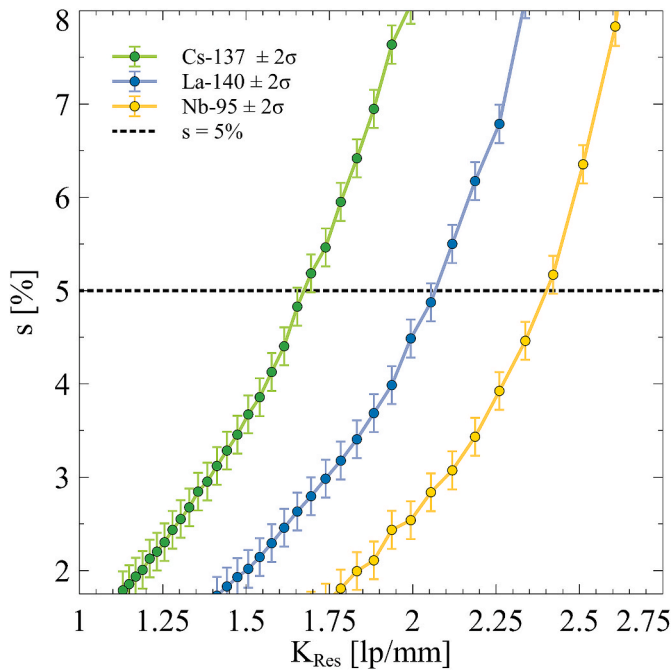


Fig. 10. The detection system proposed for BETTAN was used to evaluate the spatial resolution achievable, considering (modeled) reactor-relevant rod activity conditions. The variation of the noise levels, s , depending on the spatial resolution, K_{Res} , of the setup for a T_{Tot} of 24 h. The different colors represent the curves for the three nuclides investigated for a freshly irradiated fuel sample, Cs-137, La-140, and Nb-95. A noise level corresponding to $s = 5\%$ is reported and used as a reference.

Table 7

Summary of the performance parameter of the selected collimator solutions for a PWR high burn-up – short cooled scenario.

Parameter	Optimization study and solutions		
	Cs-137	La-140	Nb-95
Collimator material	Densimet® 180 – D180		
Unsharpness - U	0.1–0.8 mm		
Collimator length - L_C	200–350 mm		
Central counts - P	50–1500	50–2000	50–3000
Time constraint - T_{Tot}	24 h		
SBR constraint	>1000		
Noise level - s	5%		
Number of segments - N_{Det}	6		
Total measurement steps - N_{Tot}	35400	48706	62800
Data collection time - T_{Col}	~10 s	~6 s	~3 s
Spatial resolution - K_{Res}	1.6 lp/mm	2.0 lp/mm	2.4 lp/mm
Slit design selected - $w_C \times h_C \times L_C$	$0.16 \times 6.6 \times 278$ mm	$0.13 \times 6.5 \times 270$ mm	$0.12 \times 6.5 \times 258$ mm

The detector model represents a demonstrative device and presents some compromises in terms of performance. Therefore, novel detector designs, such as the ones proposed in Refs. [10,21] or the combinations of multiple-segmented detectors [51,52], are expected to improve the technique even further.

6. Conclusions and outlook

In this work, a methodology to evaluate the performance of a novel collimated gamma spectroscopy device was presented and used to propose an optimal collimator design for GET applications. Four performance metrics (total investigation time, spatial resolution, reconstruction noise, and signal-to-background ratio) have been used in

optimization routines. Since trade-offs between the objectives have been identified, Pareto optimal solutions were considered, presenting non-dominated design options.

Optimizing a multi-slit collimator planned to be used in the BETTAN tomography test bench to test a novel segmented HPGe at Uppsala University resulted in a collimator made of steel S355 with a slit cross-section of 0.7x6 mm and a length of 220 mm. We expect that with such a setup, a full investigation could be performed in about 24 h, with an SBR above 100, a noise level of about 3%, and a spatial resolution of about 0.37 lp/mm (able to resolve features in the order of 1.4 mm). The study also suggests that the spatial resolution can be improved to 0.43 lp/mm for the same reconstruction noise by reducing the slit width to 0.6 mm and increasing the investigation time to 48 h. Therefore, the method also gives further indications to the designers to improve the performance by acting on the setup design.

The study also evaluates the performance of the main planned application of the detector in GET of irradiated nuclear fuel. Three gamma-emitter nuclides (Cs-137, La-140, and Nb-95) and the respective emission lines have been used to predict the spatial resolution obtainable. The study suggests that activity variations in the fuel of about 310 μ m are expected to be resolved for Cs-137, with a full investigation of 24 h, a 30% contrast, and a maximum of 5% in the reconstructed noise level. For La-140 and Nb-95, the predicted resolution achievable is better, to 250 μ m and 210 μ m, thanks to their higher activity. This possibility represents an attractive NDA application in PIE of nuclear fuel to save time and costs for the investigation. The method is also valuable for planning GET investigations in PIE measurement campaigns by quantifying the expected performance.

As an outlook, the multi-slit collimator planned for use in BETTAN is under preparation. The operation of the tomographic test bench is ongoing to demonstrate the use of a segmented HPGe detector. In addition to this, the collimator design indicated in the study may be tested to provide experimental validation of predictions of the optimized performance presented here. This is to investigate the agreement between the ideal spatial resolution predicted using the multivariate problem proposed with the yield degradation expected in a real setup. Further on, the detector is available for use in PIE, for studies of nuclear fuel behavior, with the anticipated limit in spatial resolution near 300 μ m, as concluded in this work. However, it should be noted that a next-generation detector with more segments and a larger active volume, as suggested in Refs. [10,21] could anticipate further progress toward an even better resolution.

In the future, the use and planning of GET examinations will be facilitated by the methods presented here to know beforehand the performance that can be obtained, considering the primary metrics of interest, spatial resolution, time requirements for the acquisition, and the noise in the reconstruction pixels. In addition, the presented methods allow for selecting the best collimator for a particular fuel test and nuclide of interest.

Declaration of competing interest

The authors declare that they have no known competing financial interests or personal relationships that could have appeared to influence the work reported in this paper.

Data availability

Data will be made available on request.

Acknowledgment

This work was financially supported by the Swedish Foundation for Strategic Research, grant number EM-16-0031.

Appendix A

The derivation of the geometrical parameters of the setup is shown in this appendix. The first regards the unsharpness, U . It can be derived from trigonometrical relations in the setup (as shown in Fig. 11), considering the collimator width, w_C , length, L_C , and the distance between the source center and the collimator, d_{CS} :

$$U = w_C + 2x_S = w_C + 2\left(\frac{w_C d_{CS}}{L_C}\right) = \frac{w_C(2d_{CS} + L_C)}{L_C} \quad (13)$$

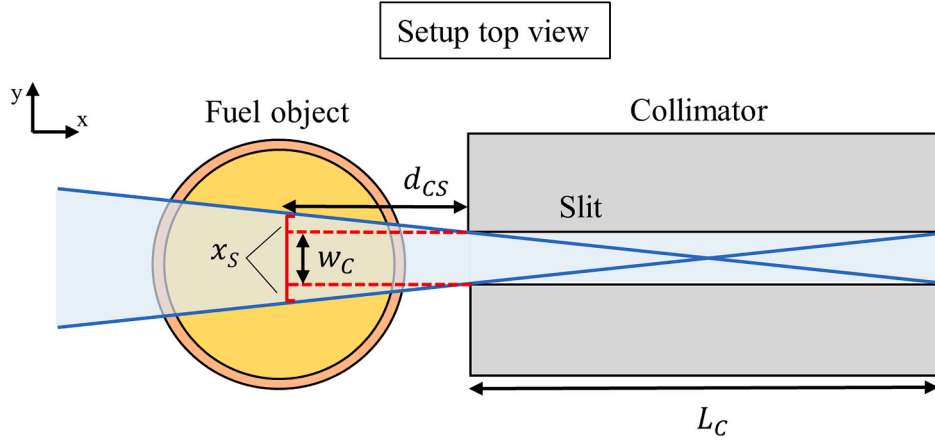


Fig. 11. Schematic representation of the setup showing the geometrical parameters influencing the setup's unsharpness.

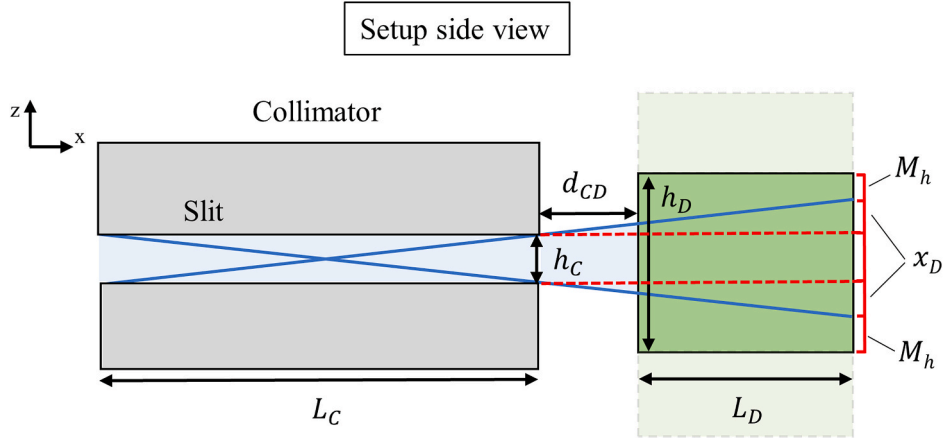


Fig. 12. Schematic representation of the setup showing the geometrical parameters influencing the collimator slit's height, h_C .

Using the detector segment height, h_D , as a boundary for the beam divergence (as shown in Fig. 12), the slit height, h_C , can be calculated considering the collimator-detector distance, d_{CD} , the detector segment length, L_D and a margin to account for possible vertical misalignment, $2M_h$:

$$h_D = h_C + 2x_D + 2M_h = h_C + 2\left(\frac{h_C(d_{CS} + L_D)}{L_C}\right) + 2M_h = h_C\left(\frac{L_C + 2(d_{CS} + L_D)}{L_C}\right) + 2M_h \quad (14)$$

The slit height is then extrapolated as:

$$h_C = \frac{(h_D - 2M_h) L_C}{L_C + 2(d_{CD} + L_D)}. \quad (15)$$

Appendix B

Summary of the model parameters and how they have been treated in the current methodology.

Device/method component	Parameter	How has been treated in the method?	
		BETTAN	PIE fuel case
Detector	Detector technology	Solid state gamma detector - HPGe	
Setup dimensions	Detector dimensions	Optimized in a dedicated study in Ref. [22]	
	Collimator-source distance	About 30 mm (assumed based on past setups)	
	Collimator-detector distance	About 20 mm (assumed based on past setups)	
Source characteristics	Activity	3.04E+07 Bq/cm (Cs-137, mean activity per mockup rod)	2.29E+10 Bq/cm (Cs-137, PWR fuel with 46 GWd/tU, and 14 days of cooling time)
	Materials	Copper and titanium cladding	UO ₂ and Zircalloy-4 cladding
	Source radius	5.25 mm	4.1 mm
	Cladding radius	6 mm	4.7 mm
Collimator	Slit dimensions	Optimized in the current study	
	Material	Structural steel	
Measurement settings	Measurement time	Optimized in the current study	
	Movement time	5 s (measured in BETTAN)	
	Lateral step	Optimized in the current study	
	Rotational step	Optimized in the current study	
Performance constraint	Signal to background	>100	>1000
Spatial resolution limit	Michelson contrast	30% (upper limit of Ref. [29])	

References

- [1] P. Jansson, S. Jacobsson Svård, A. Håkansson, A. Bäcklin, A device for nondestructive experimental determination of the power distribution in a nuclear fuel assembly, *Nucl. Sci. Eng.* 152 (1) (2006) 76–86, <https://doi.org/10.13182/NSE06-A2565>.
- [2] S. Holcombe, S. Jacobsson Svård, L. Hallstadius, A novel gamma emission tomography equipment for enhanced fuel characterization capabilities within the OECD Halden Reactor Project, *Ann. Nucl. Energy* 85 (2015) 837–845, <https://doi.org/10.1016/j.anucene.2015.06.043>.
- [3] C. Willman, A. Håkansson, O. Osifo, A. Bäcklin, S. Jacobsson Svård, Nondestructive assay of spent nuclear fuel with gamma-ray spectroscopy, *Ann. Nucl. Energy* 33 (5) (2005) 427–438, <https://doi.org/10.1016/j.anucene.2005.12.005>.
- [4] J. Schulthess, N. Woolstenhulme, A. Craft, J. Kane, N. Boulton, W. Chirazzi, A. Winston, A. Smolinski, C. Jensen, D. Kamerman, D. Wachs, Non-Destructive post-irradiation examination results of the first modern fueled experiments in TREAT, *J. Nucl. Mater.* 541 (2020), 152442, <https://doi.org/10.1016/j.jnucmat.2020.152442>.
- [5] D.M. Wachs, Transient testing of nuclear fuels and materials in the United States, *J. Occup. Med.* 64 (12) (2012) 1396–1402, <https://doi.org/10.1007/s11837-012-0482-2>.
- [6] S. Caruso, F. Jatuff, Design, development and utilisation of a tomography station for γ -ray emission and transmission analyses of light water reactor spent fuel rods, *Prog. Nucl. Energy* 72 (2014) 49–54, <https://doi.org/10.1016/j.pnucene.2013.09.007>.
- [7] J.M. Harp, P.A. Demkowicz, Investigation of the Feasibility of Utilizing Gamma Emission Computed Tomography in Evaluating Fission Product Migration in Irradiated TRISO Fuel Experiments, United States, 2014. URL: <https://www.osti.gov/servlets/purl/1167534>.
- [8] B. Biard, Quantitative analysis of the fission product distribution in a damaged fuel assembly using gamma-spectrometry and computed tomography for the Phébus FPT3 test, *Nucl. Eng. Des.* 262 (2013) 469–483, <https://doi.org/10.1016/j.nucengdes.2013.05.019>.
- [9] J. Navarro, T.A. Ring, D.W. Nigg, Gamma-ray simulated spectrum deconvolution of a LaBr3 1- \times 1-in. Scintillator for nondestructive ATR fuel burnup on-site predictions, *Nucl. Technol.* 190 (2) (2015) 183–192, <https://doi.org/10.13182/NT14-4>.
- [10] P. Andersson, V. Rathore, L. Senis, A. Anastasiadis, E. Andersson Sundén, H. Atak, S. Holcombe, A. Håkansson, P. Jansson, J. Nyberg, Simulation of the response of a segmented high-purity germanium detector for gamma emission tomography of nuclear fuel, *SN Appl. Sci.* 2 (2) (2020) 271, <https://doi.org/10.1007/s42452-020-2053-4>.
- [11] M. Fang, Y. Altmann, D. Della Latta, M. Salvatori, A. Di Fulvio, Quantitative imaging and automated fuel pin identification for passive gamma emission tomography, *Sci. Rep.* 11 (1) (2021) 2442, <https://doi.org/10.1038/s41598-021-82031-8>.
- [12] P. Andersson, S. Holcombe, A computerized method (UPPREC) for quantitative analysis of irradiated nuclear fuel assemblies with gamma emission tomography at the Halden reactor, *Ann. Nucl. Energy* 110 (2017) 88–97, <https://doi.org/10.1016/j.anucene.2017.06.025>.
- [13] S. Shiba, H. Sagara, Iterative reconstruction algorithm comparison using Poisson noise distributed sinogram data in passive gamma emission tomography, *J. Nucl. Sci. Technol.* 58 (6) (2021) 659–666, <https://doi.org/10.1080/00223131.2020.1854882>.
- [14] P. Andersson, S. Halcombe, Inspection of a LOCA test rod at the halden reactor project using gamma emission tomography, in: *Top Fuel (Light Water Reactor Fuel Performance Meeting)*, Boise, Idaho, USA, 2016. URL: <http://urn.kb.se/resolve?urn=urn:nbn:se:uu:diva-303810>.
- [15] NUCLEAR ENERGY AGENCY, *Nuclear Fuel Behaviour in Loss-Of-Coolant Accident (LOCA) Conditions*, 2009. NEA No. 6846.
- [16] S. Holcombe, P. Andersson, in: *Top Fuel*, I.D. Boise (Eds.), Gamma Emission Tomography Measurements of Fuel Assemblies at the Halden Reactor, 2016. URL: <http://urn.kb.se/resolve?urn=urn:nbn:se:uu:diva-303812>.
- [17] L. Senis, V. Rathore, P. Andersson, K. Johnson, D. Jäderås, C. Losin, D. Minghetti, J. Wright, D. Schrire, Performance evaluation of a novel gamma transmission micro-densitometer for PIE of nuclear fuel, *Ann. Nucl. Energy* 187 (2023), 109783, <https://doi.org/10.1016/j.anucene.2023.109783>.
- [18] S. Kilby, J. Fletcher, A. Avachat, Z. Jin, D. Imholte, N. Woolstenhulme, H.K. Lee, J. Graham, Multi-modal tomographic imaging system for poolside characterization of nuclear test fuels: design considerations and studies, *Nucl. Instrum. Methods Phys. Res. Sect. A Accel. Spectrom. Detect. Assoc. Equip.* 1045 (2023), 167553, <https://doi.org/10.1016/j.nima.2022.167553>.
- [19] J. Legriel, C. Le Guernic, S. Cotton, O. Maler, Approximating the Pareto Front of Multi-Criteria Optimization Problems, 2010, pp. 69–83, https://doi.org/10.1007/978-3-642-12002-2_6.
- [20] P. Jansson, S. Jacobsson Svård, S. Grape, A. Håkansson, A laboratory device for developing analysis tools and methods for gamma emission tomography of nuclear fuel, in: *ESARDA Symposium 2013 35th Annual Meeting*, Bruges, Belgium, 2013. URL: http://publications.jrc.ec.europa.eu/repository/bitstream/JRC83924/lcna_26127enn.pdf.
- [21] V. Rathore, L. Senis, E. Andersson Sundén, P. Jansson, A. Håkansson, P. Andersson, Geometrical optimisation of a segmented HPGe detector for spectroscopic gamma emission tomography—a simulation study, *NIM A: Accelerators, Spectrometers, Detectors and Associated Equipment* 998 (2021), 165164, <https://doi.org/10.1016/j.nima.2021.165164>.
- [22] V. Rathore, L. Senis, P. Jansson, E. Andersson, Sundén A. Håkansson, P. Andersson, Calculations of the spatial response of a collimated segmented HPGe detector for gamma emission tomography by MCNP simulations, *IEEE Trans. Nucl. Sci.* 69 (4) (2022) 714–721, <https://doi.org/10.1109/TNS.2022.3152056>.
- [23] F. Khari, Mathematics and physics of computed tomography (CT): demonstrations and practical examples, in: *Imaging and Radioanalytical Techniques in Interdisciplinary Research - Fundamentals and Cutting Edge Applications*, IntechOpen, 2013, <https://doi.org/10.5772/52351>.
- [24] L. Senis, V. Rathore, A. Anastasiadis, E. Andersson Sundén, Z. Elter, S. Holcombe, A. Håkansson, P. Jansson, D. LaBrier, J. Schulthess, P. Andersson, Evaluation of Gamma-Ray Transmission through Rectangular Collimator Slits for Application in Nuclear Fuel Spectrometry, 1014, *Spectrometers, Detectors and Associated Equipment*, 2021, 165698, <https://doi.org/10.1016/j.nima.2021.165698>. NIM A: Accelerators.
- [25] L. Senis, Z. Elter, V. Rathore, E. Andersson Sundén, P. Jansson, S. Holcombe, M. Åberg Lindell, A. Håkansson, P. Andersson, A computational methodology for estimating the detected energy spectra of the gamma-ray flux from irradiated nuclear fuel, *IEEE Trans. Nucl. Sci.* 69 (4) (2022) 703–713, <https://doi.org/10.1109/TNS.2022.3152264>.
- [26] G.L. Zeng, Detector blurring and detector sensitivity compensation for a spinning slit collimator, *IEEE Trans. Nucl. Sci.* 53 (5) (2006) 2628–2634, <https://doi.org/10.1109/TNS.2006.882574>.
- [27] R.L. Wildey, The nyquist criterion in CCD photometry for surface brightness, *Publ. Astron. Soc. Pac.* 104 (674) (1992) 285–289. URL: <https://www.jstor.org/stable/40679860>.
- [28] R. Srinivasan, D.M. Tucker, M. Murias, Estimating the spatial Nyquist of the human EEG, *Behav. Res. Methods Instrum. Comput.* 30 (1) (1998) 8–19, <https://doi.org/10.3758/BF03209412>.

- [29] J. Diaz, T. Kim, V. Petrov, A. Manera, X-ray and gamma-ray tomographic imaging of fuel relocation inside sodium fast reactor test assemblies during severe accidents, *J. Nucl. Mater.* 543 (2021), 152567, <https://doi.org/10.1016/j.jnucmat.2020.152567>.
- [30] B. Moulden, F. Kingdom, Linda F. Gatley, The standard deviation of luminance as a metric for contrast in random-dot images, *Perception* 19 (1) (1990) 79–101, <https://doi.org/10.1068/p190079>.
- [31] C.J. Werner, *MCNP(R) User's Manual Coder*, 2017. Version 6.2.
- [32] W. van Aarle, W.J. Palenstijn, J. Cant, E. Janssens, F. Bleichrodt, A. Dabrovolski, J. De Beenhouwer, K.J. Batenburg, J. Sijbers, Fast and flexible X-ray tomography using the ASTRA toolbox, *Opt Express* 24 (2016) 25129–25147, <https://doi.org/10.1364/OE.24.025129>.
- [33] W. van Aarle, W.J. Palenstijn, J. De Beenhouwer, T. Altantzis, S. Bals, K. J. Batenburg, J. Sijbers, The ASTRA Toolbox: a platform for advanced algorithm development in electron tomography, *Ultramicroscopy* 157 (2015) 35–47, <https://doi.org/10.1016/j.ultramic.2015.05.002>.
- [34] S. Rehbein, P. Guttman, S. Werner, G. Schneider, Characterization of the resolving power and contrast transfer function of a transmission X-ray microscope with partially coherent illumination, *Opt Express* 20 (6) (2012) 5830–5839, <https://doi.org/10.1364/OE.20.005830>.
- [35] X. Li, et al., Real-time denoising enables high-sensitivity fluorescence time-lapse imaging beyond the shot-noise limit, *Nat. Biotechnol.* (2022) 1–11, <https://doi.org/10.1038/s41587-022-01450-8>.
- [36] G.R. Gilmore, *Practical Gamma-Ray Spectroscopy*, Wiley: Wiley, Nuclear Training Services Ltd, Warrington, UK, 2008.
- [37] G.F. Knoll, *Radiation Detection and Measurement*, Wiley, New York, 1979.
- [38] D.M. Pelt, Doctoral Thesis: Filter-Based Reconstruction Methods for Tomography, Utrecht, 2016. URL: <https://hdl.handle.net/1887/39638>.
- [39] C.E. Rasmussen, C.K.I. Williams, *Gaussian Processes for Machine Learning*, The MIT Press, 2006, <https://doi.org/10.7551/mitpress/3206.001.0001>.
- [40] L.F. Pires, F.A.M. Cássaro, L. Tech, L.A.A. Pereira, J.A.T. de Oliveira, Gamma ray attenuation for determining soil density: laboratory experiments for Environmental Physics and Engineering courses, *Rev. Bras. Ensino Física* 42 (2020), <https://doi.org/10.1590/1806-9126-RBEF-2019-0340>.
- [41] M.S. Gossman, A.J. Pahikkala, M.B. Rising, P.H. McGinley, Letter to the editor, *J. Appl. Clin. Med. Phys.* 12 (1) (2011) 242–243, <https://doi.org/10.1120/jacmp.v12i1.3530>.
- [42] H. Choi, B. Cheon, M. Kyubaek, H. Chung, Y.H. Chung, S.H. You, C.H. Min, H. J. Choi, Experimental evaluation of fuel rod pattern analysis in fuel assembly using Yonsei single-photon emission computed tomography (YSECT), *Nucl. Eng. Technol.* 54 (6) (2022) 1982–1990, <https://doi.org/10.1016/j.net.2021.12.035>.
- [43] S. Jacobsson Svård, *A Tomographic Measurement Technique for Irradiated Nuclear Fuel Assemblies*, Acta Universitatis Upsaliensis, Uppsala, Sweden, 2004. URL: <http://urn.kb.se/resolve?urn=urn:nbn:se:uu:diva-4227>.
- [44] V. Mishra, Z. Elter, E. Branger, S. Grape, Statistical analysis of fuel cycle data from Swedish pressurized water reactors and the impact of simplifying assumptions on simulated nuclide inventories, SSRN Scholarly Paper (2022), <https://doi.org/10.2139/ssrn.4108868>.
- [45] J. Leppänen, M. Pusa, T. Viitanen, V. Valtavirta, T. Kaltiaisenaho, The Serpent Monte Carlo code: status, development and applications in 2013, *Ann. Nucl. Energy* 82 (2015) 142–150, <https://doi.org/10.1016/j.anucene.2014.08.024>.
- [46] H. Takiishi, J.H. Duvaizen, I.M. Sato, J.L. Rossi, L.A.T. Pereira, L.G. Martinez, Recycling of zircaloy machining chips by VAR remelting and powder metallurgy techniques, *Mater. Sci. Forum* 727 (728) (August 2012) 356–361, <https://doi.org/10.4028/www.scientific.net/MSF.727-728.356>.
- [47] R. Khan S. Karimzadeh, H. Böck, TRIGA fuel burn-up calculations and its confirmation, *Nucl. Eng. Des.* 240 (5) (2010) 1043–1049, <https://doi.org/10.1016/j.nucengdes.2010.01.009>.
- [48] I. Matssona, B. Grapengiesser, The shut-down of the Barsebäck 1 BWR: a unique opportunity to measure the power distribution in nuclear fuel rods, *Ann. Nucl. Energy* 33 (13) (2006) 1091–1101, <https://doi.org/10.1016/j.anucene.2006.07.007>.
- [49] C. de Boor, *A Practical Guide to Splines*, Springer-Verlag, New York, 1978.
- [50] DENSIMET® and INERMET® tungsten heavy alloys, URL: http://www.ultrasonic-resonators.org/misc/references/articles/Plansee_densimet-inermet.pdf.
- [51] T. Honkamaa, F. Levai, R. Berndt, P. Schwalbach, S. Vaccaro, A. Turunen, *A Prototype for Passive Gamma Emission Tomography*, International Atomic Energy Agency (IAEA), 2015 (IAEA-CN-220).
- [52] T. White, A. Lebrun, T. Honkamaa, M. Mayorov, P. Peura, J. Dahlberg, J. Keubler, V. Ivanov, Asko Turunen, Application of passive gamma emission tomography (PGET) for the verification of spent nuclear fuel, in: 59th Annual Conference of the Institute of Nuclear Materials Management, Baltimore, MD, USA, 2018.